Identication of the Crushing Behavior of Brittle Foam: From Indentation to Oedometric Tests

Amine Bouterf, Jérôme Adrien, Eric Maire, Xavier Brajer, Francois Hild, Stéphane Roux

Identification of the Crushing Behavior of Brittle Foam: From Indentation to Oedometric Tests

A. Bouterf[a,c,*], J. Adrien[b], E. Maire[b], X. Brajer[c], F. Hild[a], S. Roux[a]

[a] *Laboratoire de Mécanique et Technologie*
ENS Cachan/CNRS/Université Paris-Saclay, Cachan, France
[b] *MATEIS, INSA-Lyon / CNRS, Villeurbanne, France*
[c] *Saint-Gobain Recherche, Aubervilliers Cedex, France*

Abstract

Compaction of the core of plasterboard is one of the limiting phenomena for its mechanical performance. This mechanism is studied herein in an indentation test. A cylinder made of foamed gypsum is indented *in-situ* in an X-ray lab tomograph with a sphere of millimeter radius. The reported experiments show that foamed plaster displays a sharp transition between an undamaged state (with linear elastic behavior) and a compacted state with collapsed porosity under the indenter. Tomographic acquisitions of the sample under load associated with a global version of Digital Volume Correlation allow displacement fields to be measured at different load levels. However, because of the heterogeneous nature of the indentation test, a fine spatial resolution of the displacement fields is required to measure the strains at the crush-

*Corresponding Author. Fax: +33 1 47 40 22 40
Email addresses: bouterf@lmt.ens-cachan.fr (A. Bouterf), jerome.adrien@insa-lyon.fr (J. Adrien), eric.maire@insa-lyon.fr (E. Maire), xavier.brajer@saint-gobain.com (X. Brajer), hild@lmt.ens-cachan.fr (F. Hild), stephane.roux@lmt.ens-cachan.fr (S. Roux)

ing limit. A dedicated procedure exploiting computed displacement fields within the digital volume correlation procedure is utilized. It allows for the quantification of stress fields that are post-processed to identify the crushing criterion. It is shown that this analysis is very consistent with more macroscopic oedometric tests. Last, predictions of a Mohr-Coulomb model are compared with macroscopic and microscopic data. It is shown that despite the fact that this model reproduces very well the load-displacement response of the indentation test, a poorer prediction of the experimental crushed zone is observed. In particular, the transition between compacted plaster and its pristine state is not captured by the model, which predicts a very progressive transition rather than an abrupt one. The same conclusions are drawn for a crushable foam model when compared with experimental evidence of an *in-situ* oedometric test.
Keywords: A. Indentation and hardness, B. Foam material, C. Mechanical testing, D. Computed tomography

---

1. Introduction

Since its invention by A. Sackett in 1894, the manufacturing process of plasterboard has been steadily improved to meet ever more stringent standards. The current trend consists of decreasing the weight of plasterboard (i.e., producing a sandwiched structure made of foamed plaster core, dense plaster roller coating and paper skin) to offer a better compromise of conflicting properties (thermal and acoustic insulation, fire resistance and mechanical strength), and simultaneously reducing energy consumption for its fabrication and transportation. Even though plasterboard is extensively utilized in the construction sector, very few studies are devoted to the evaluation of mechanical properties of such sandwiched structures in which the core is made of brittle foam.

Failure modes of sandwiches may have different forms depending on the type of loading, geometry and mechanical properties of its components. The most commonly observed modes are [1]:

- Indentation at the loading point; the failure mechanism is a consequence of the localized nature of loading. In flexural tests, it is possible to observe this phenomenon at the supports.

- Skin rupture; the skin may be broken if it is stressed beyond its strength.

- Folding of the skin; during a compression test, the skin may buckle.

- Core failure; it usually occurs in tension and shear.

- Skin debonding; adhesion between the roller coating and the skin can be broken.

When analyzing the behavior of plasterboard in the standardized nail-pull test, it has been suggested via *in-situ* tomography that core crushing was the prevalent failure mechanism [6, 13]. However, the nail-pull test has a complex geometry, and due to the intricate parts played by the composite structure (paper facing, roller coating, foam core), it is difficult to isolate one key phenomenon. This study aims to provide a more thorough analysis of the core crushing phenomenon through simpler mechanical tests and in particular spherical indentation via *in-situ* test in a lab tomograph.

Indentation has been widely used to characterize highly porous materials such as metal foams [16]. Unlike dense ductile materials, the area affected by indentation in metal or polymer foams is limited to a densified region near the indenter. Another difference is the violation of the classical relationship between the hardness (i.e., mean indentation stress) and the yield stress. The ratio of the average indentation stress and the yield stress is close to 3 for metals [34] and tends to 1 for cellular materials [38]. According to Bart-Smith *et al.* [2], it is related to the tendency of materials with a high porosity not to deform laterally because of Poisson's effect, which limits the effect of yielding under the indenter.

Indentation has also been described by Gibson and Ashby [16] for both ductile and brittle foams. The authors consider that the indentation of a foam, contrary to that of a dense material, is not a true multiaxial test. The effective Poisson's ratio close to zero during crushing means that the material undergoes simple compression. Olurin *et al.* [27] have characterized the indentation resistance of metal foams for different indenter geometries. The deformation of aluminum foams is exclusively controlled by the area

directly below the indenter. This is related to the absence of lateral spread of strains (i.e., near zero Poisson's ratio) [11]. The rest of the sample remains in an elastic regime. The shape of the densified zone is in both cases of indenters (i.e., spherical and flat) hemispherical. The flat indenter leads to a compacted volume greater than that obtained with a spherical indenter. Such a phenomenon with a comparable form of compacted area has been observed in a refractory material with 65 % of porosity [33], an artificial porous rock [21] and aluminum foams [3, 32]. Similar observations have been reported for porous plaster [4, 9, 10].

Some work was also carried out by registering X-ray tomographies via digital volume correlation (DVC) to study the kinematics during the penetration of a conical tip into a silty soil sample [28]. Strain localization in granular media and the link between grain angularity and grain rotation within shear bands have been reported [12, 17]. Forsberg and Siviour [14] studied the compaction mechanism of a cylindrical bed of sugar. Recently, *in-situ* X-ray computed tomography coupled with DVC has been used to characterize the fracture behavior of quasi-brittle materials [24, 25] and the 3D opening modes and displacements of indentation-initiated cracks in a brittle ceramic [36]. Mostafavi *et al.* [23] demonstrated that plastic material properties of a ductile metal, i.e., yield stress and hardening exponent, can be extracted by inverse analysis of the displacement field below a hardness indentation measured by DVC of *in-situ* tomographic observations.

There are fewer studies dealing with brittle foams. In particular, virtually no results have been reported for plaster. The present paper aims to analyze an indentation test to assess the transition from intact elastic plaster

to a crushed state. As this process takes place under the indenter, surface observations do not give insight into this process. Consequently, *in-situ* indentation will be monitored within a lab tomograph (Section 2). Once the 3D volumes have been reconstructed, it is then possible to analyze the failure mechanism. Section 3 proposes a minimal constitutive law that reproduces the most salient features of the indentation test. Using Digital Volume Correlation (DVC), it is possible to quantitatively evaluate displacement fields (Section 4). In the present case, very small strain levels are sought and indentation induces heterogeneous strain and stress fields with a rapid decay with distance away from the indenter. These two features have prompted to the introduction of a reduced basis [5] that is used to evaluate the stresses at the boundary between the pristine and crushed material. These stresses give access to a measurement of the Rankine limit, which is consistent with the analysis of the indentation response (Section 5). Further, macroscopic oedometric tests (Section 6) are performed to confirm the previous analyses at a larger scale. These different experiments validate quite consistently a simple constitutive law able to account for crushing of brittle foams in general, and of the studied plaster in particular. Conversely, two classical models (i.e., Mohr-Coulomb and crushable foam) are shown to be consistent with load-penetration data but not with microscopic observations of the *in-situ* indentation test (Section 7).

2. *In-situ* Indentation Test

Lightweight gypsum is made of a plaster foam core whose porosity can reach 75 % (as in the present case) and board skins. The main function of

the two paper skins is to bear tensile stresses and protect the core of the sandwiched plate bridging transverse cracks. For light boards, an additional dense plaster layer (i.e., the so-called roller coating) between the core and the skins proves to be beneficial for higher stiffness and better bonding with the paper facings. Figure 1(a) shows a tomographic section revealing the different components of lightweight plasterboard observed at a fine resolution of 1.4 μm. This very good image of the initial state of the sample (in terms of resolution and signal to noise ratio) was obtained using synchrotron (ESRF beamline ID19) data.

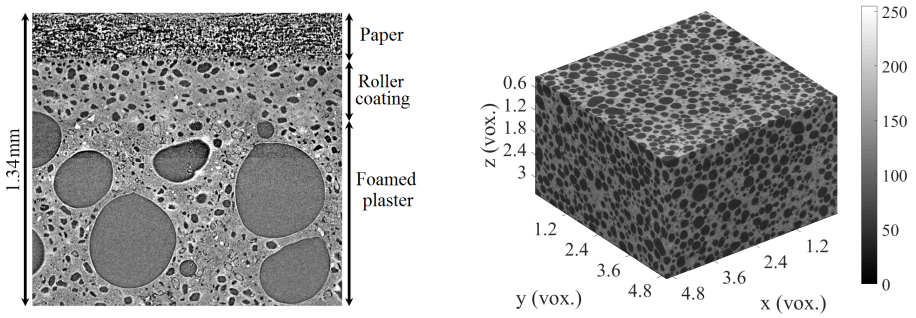

(a) (b)

Figure 1: (a) Tomographic section showing the microstructure observed at a resolution of 1.4 μm of the studied plaster whose porosity is of the order of 75 %. The size of the section is 1.34×1.4 mm^2. (b) 3D rendering of the microstructure of the core material studied herein and observed at a resolution of 12 μm. The size of the volume is $4.8 \times 4.8 \times 3.2$ mm^3

The core foam sample used in the experiment reported hereafter was cut from an industrial plasterboard. The upper paper and the roller coating were removed using an electric planer. Plaster foam specimens are 17-mm diameter and 10-mm thick cylinders, which are extracted from the core foam with an annular cutter. The upper surface of the samples is flat, smooth and

without apparent densification. Figure 1(b) shows the material microstructure at a resolution of 12 μm, in the form of a gray level slice parallel to the board. A 6 mm in diameter spherical glass indenter is chosen. The *in-situ* indentation test is quasi-static with an indenter speed of 5 μm/s. The experimental setup is shown in Figure 2(a). The standard *in-situ* compression rig described in Ref. [8] is used.

The sample was imaged in the initial state (i.e., no applied load) and for several levels of compressive loading. After each load increment, the crosshead is stopped and the next scan is acquired after a dwell time of about 20 minutes to avoid image blur due to the motion of the sample during the relaxation process. The experiments were conducted in a laboratory tomograph described in Ref. [7] with the following acquisition parameters: 90-kV beam voltage, 200-μA electron current, 12-μm resolution. 900 radiographs are acquired over a 360° rotation for each scan. The total duration of a single scan is about 35 minutes. Figure 2(b) shows a photograph of the sample prepared from the plate before and after indentation.

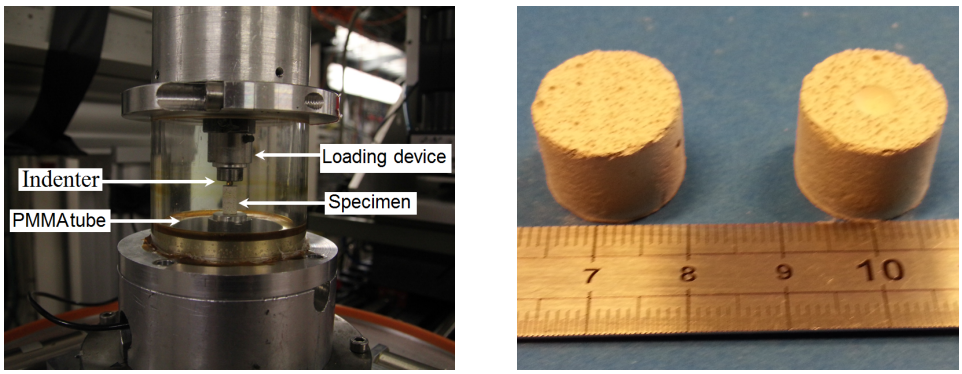

(a) (b)

Figure 2: (a) *In-situ* indentation test. (b) Sample prior to and after the indentation test

Figure 3(a) shows three load-displacement curves of indentation tests of the studied foamed plaster. Even though foamed plaster has a coarse microstructure (Figure 1) its macroscopic response does not exhibit large fluctuations. This result shows that indentation tests at the scale chosen herein (i.e., plaster foam shown in Figure 1 and 6 mm in diameter spherical indenter) are repeatable. The following analyses will focus on a single test. For the in-situ experiment the applied load and corresponding displacement were recorded and controlled during the test. Figure 3(b) shows the load/displacement history of the indenter. The oscillations in the response curve were attributed to repeated events of porosity collapse and densification during loading. A similar dependence of the applied force with penetration depth was obtained for porous rocks [21], cemented carbide [26], and plaster [10].

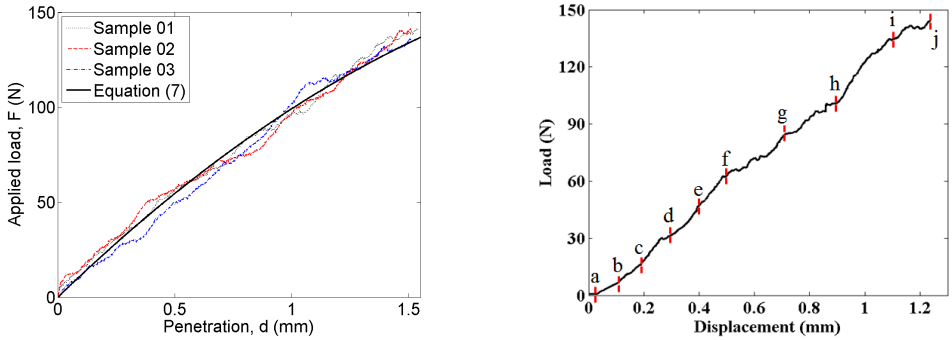

(a) (b)

Figure 3: (a) Load-displacement curves of three indentation tests on the studied foamed plaster. (b) Load-displacement curve of the analyzed in-situ indentation test. The letters on the graph indicate the load levels at which a tomographic scan has been acquired

Figure 4(a) shows a frontal section of scan j. A densified region (i.e.,

where the coarse porosity is no longer present) is clearly seen under the indenter. Away from this region, the structure of the foam appears as being unaltered. The interface between the crushed and undamaged zone appears to be extremely sharp.

3. Two-Phase Modeling

The sharpness of the interface suggests that the foam behavior consists of a softening (and hence unstable) part separating a linear elastic regime (fully reversible) that is coined "E" as elastic in the following, from a fully crushed state (denoted as "C"). In state C the solid walls separating bubbles have been broken down to small pieces filling in the original mesoporosity so that the crushed state can be seen at larger scales as a homogeneous granular medium. The microstructure of the foam (i.e., at the micropore scale, see Figure 1) is fully destroyed in this crushed state. It is expected that very small (i.e., sub-micrometric) scale plaster will preserve a significant microporosity between gypsum microcrystals, but the latter is inaccessible in the experimental set-up used in this study; this crushed state will be considered as mechanically incompressible.

It is well-known that such a softening branch in the stress-strain law cannot be measured as it leads to an instability for a homogeneously loaded specimen. The crushed phase is expected to progressively invade the sample, with a coexistence between the two states separated by sharp interfaces where a transition criterion (i.e., brittle failure of the foam) is reached. For a homogeneous test, uniqueness is generally lost and many possible distributions of the two phases (E and C) are admissible.

Spherical indentation however does not suffer from the same degeneracy. Since stresses are progressively decreasing as one moves away from the indenter, the transition from undamaged to crushed states is expected to be a boundary that progresses into the specimen from the indenter. The situation is comparable to brittle fracture, namely, a finite crack in an infinite domain remotely loaded by a uniform stress propagates in an unstable manner as the stress intensity factor increases with the crack length. However, in a strong stress gradient it is possible to turn crack propagation as stable, provided the stress intensity factor decreases with the crack length. Here similarly, a compaction boundary will be naturally arrested when it will reach a stress level that corresponds to the failure of the elastic regime.

This picture naturally drives to a rather precise model for the foam plaster core. Regime E corresponds to a linear elastic regime. The distribution of bubbles is generally fully isotropic so that this regime is only characterized by Young's modulus E and Poisson's ratio ν. Because of the high porosity of the studied brittle foam, the Poisson's ratio is small (it has been measured for this material as $\nu \approx 0.15$). Region C corresponds to a cohesionless granular medium. It will not be possible to say much about the rheology of this crushed state as it is confined under the indenter. Moreover, as compared to the huge jump in strain across the C$\rightarrow$E transition, additional volumetric strains corresponding to the compaction of the crushed state can be neglected.

Last, the important feature that is responsible for most of the observed deformation is the C$\rightarrow$E transition. Considering that this transition corresponds to the collapse of mesoporosity, it is expected to correspond to a sud-

den volumetric strain that assumes a well-defined value. Because the strain is large it is necessary to consider a suited large transformation formalism. Hencky strains are chosen herein. If ϕ is the porosity that is collapsed in this transition, then the (Hencky) volumetric strain is $\Delta\epsilon_{CE} = \log(1-\phi)$. The stress level at the onset of densification is the crushing criterion discussed below.

3.1. Geometric Considerations

The geometry of the test is shown in Figure 4. The indenter is a sphere of radius R. Ignoring the contribution of elastic strain, and possible pile-up, for a penetration, d, of the spherical cap, the radius of contact, a, obeys

$$a^2 = R^2 - (R-d)^2 = 2Rd - d^2 \tag{1}$$

The densified zone is modeled as enclosed by a spherical cap domain with a radius of curvature ρ. As shown in Figure 4, the interface penetrates the sample over a distance δ. Because the crushed region intersects the free face exactly over the contact surface, which is limited by a circle of radius a, the penetration and radius are related through the same equation as that of the indenter though with a different radius of curvature, ρ

$$a^2 = 2\rho\delta - \delta^2 \tag{2}$$

The volume enclosed by the E-C boundary is $V_0 = \pi(\rho\delta^2 - \delta^3/3)$, while the volume of the indenter that has penetrated into the solid is $V_i = \pi(Rd^2 - d^3/3)$. According to the previous two-phase model, the ratio between those volumes should be equal to the porosity

$$\phi = V_i/V_0 = \frac{Rd^2 - d^3/3}{\rho\delta^2 - \delta^3/3} \tag{3}$$

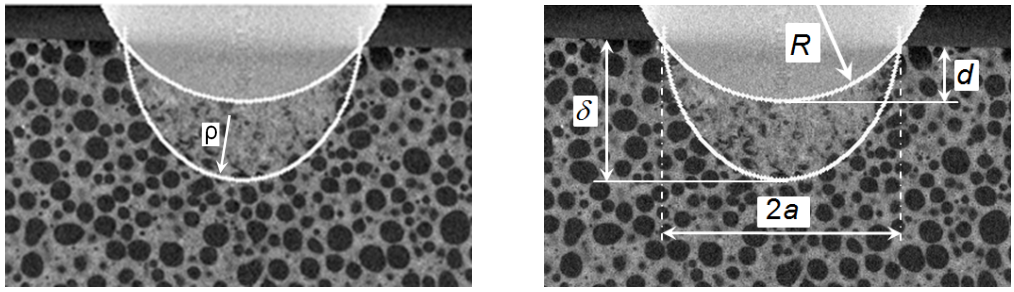

Figure 4: (a) Section of the plaster sample at stage j. The indenter is the two-shaded gray domain bounded by the top white circle. Beneath it, plaster shows a region with a rather uniform gray level (i.e., with almost no visible pores) whereas farther away the foam structure appears undamaged. The white arc of circle drawn on top of the image is a guide to the eye for the interface between these two zones. (b) Frontal section of scan (j) with different notations

From Equations (2) and (3), ρ and δ are determined from R and d. An exact solution can be expressed from a cubic equation (see Appendix A). However, in the limit of a small indentation depth, $d/R \ll 1$, these parameters assume a simple expression: $\delta = d/\phi$ and $\rho = \phi R$. It is interesting to note that the precise shape of the indenter does not play a very significant role as indentation can be seen as that of an elastic material by an *effective indenter* made out of crushed gypsum, with a reduced indenter radius, $\rho \approx \phi R$.

It is worth observing that the dimensionless ratio $a^2/(2Rd)$ takes a constant value for different indentation models. For Hertz contact, $a^2/(2Rd) = 0.5$. A ratio less than one means that the free surface is brought down further than within the contact area (i.e., "sink-in"). For an ideal rigid-perfectly plastic material (with J2 flow rule) with negligible elastic deformation, $a^2/(2Rd) = 1.43$ [20]. The fact that the ratio exceeds one, or "pile-up"

effect, is due to plastic incompressibility. In the above model of crushable foam, this ratio is also constant and equal to $a^2/(2Rd) = 1$. The absence of sink-in effect comes from negligible elastic strains, whereas pile-up does not occur since the foam is crushed in place without further flow of the comminuted material. Even though all these results only hold for low indentation depths, $d/R \ll 1$, it is interesting to note that they allow for a simple sorting of dominant effects from geometrical observations only. The following section will show that this result is in very good agreement with experimental data.

3.2. Validation from Tomographic Images

The geometrical relationship, Equation (3), is validated against direct tomographic images from which d and δ are measured at various penetration depths, and the assumption about the shape and radius of the compacted domain will be confirmed.

The microstructure changes during the test are shown in Figure 5 by frontal sections at different load levels from g to j. For smaller loads, the penetration is too small to analyze the crushed region in such sections. Crushed plaster is always located under the indenter, and a spherical cap shape as shown in the figure gives a faithful account of the observed geometry. The E-C boundary intersects the free surface precisely at the edge of the contact surface. In the E domain, the microstructure remains intact. A finer analysis (reported below) will reveal that an elastic deformation is detected and measured but no sign of damage is perceived away from the E-C boundary.

The frontal sections shown in Figure 5 for different loading levels are further exploited by measuring d and δ, so as to confront with the prediction of Equation (3). The result is shown in Table 1. It is observed that the

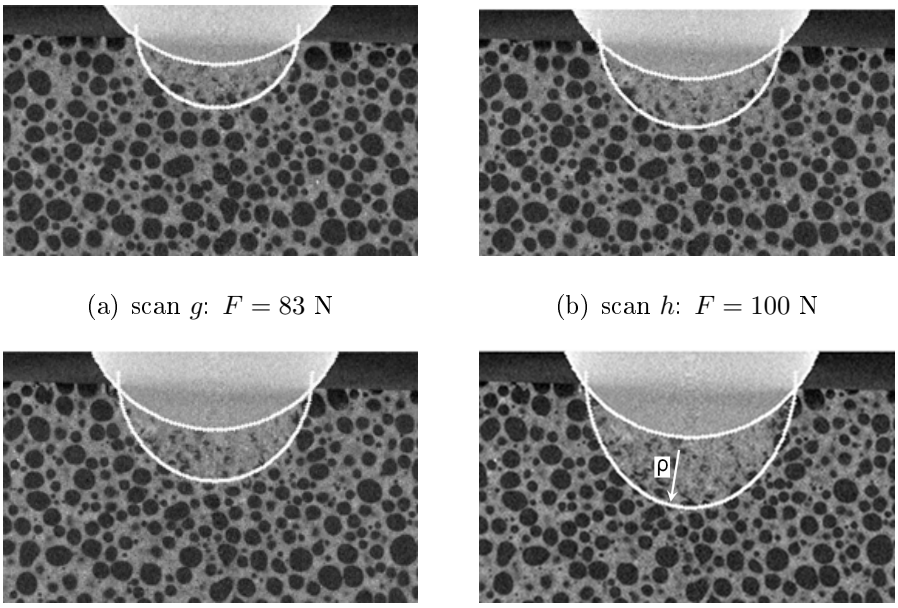

(a) scan g: $F = 83$ N

(b) scan h: $F = 100$ N

(c) scan i: $F = 135$ N

(d) scan j: $F = 145$ N

Figure 5: Frontal sections showing a zoom around the compacted region at different load levels. The densified zone is defined by a spherical cap fit. The *in-situ* observations also show that the contact radius between the indenter and the sample is the same as that of the compacted zone

porosity in the region C, ϕ, due to indentation is consistent with a constant value

$$\phi \approx 0.47 \tag{4}$$

for all considered loading steps.

3.3. Static Analysis

After penetration of the indenter in the sample, the mean stress at which the porosity collapses, which is denoted by σ_{eff}, is given by

$$\sigma_{eff} = \frac{F}{S_{cont}} = \frac{F}{\pi a^2} = \frac{F}{\pi(2Rd - d^2)} \tag{5}$$

Table 1: Measured ratio of penetration depth d to depth of the crushed region δ for different load levels. This ratio, according to the proposed model, is equal to the mesoporosity of gypsum foam

Scan	g	h	i	j
Measured d/δ	0.44	0.47	0.50	0.46

where S_{cont} is the contact surface. Hence the linear relationship between the applied load, F, and the observed penetration, d, for small d/R that is observed in Figure 3 is consistent with a constant apparent crushing strength $\sigma_{eff} = \sigma_c$

$$F = 2\pi R d \sigma_c \tag{6}$$

as long as $d/R \ll 1$.

The next question that arises is whether an interpretation can be given to this crushing strength that would be a material property. The latter has to be related to a local stress criterion for the E-C transition. A possible candidate is Rankine's criterion, which is stating that the minimum principal stress σ_{min} cannot be less than $-\sigma_R$. As the foam is crushed to a comminuted material, no shear flow is expected and hence at the E-C boundary the normal to the interface is a principal stress direction, which is carrying the major compressive stresses, hence equal to the Rankine stress $-\sigma_R$. With this assumption, the applied load is calculated from an integration over the E-C interface S becomes

$$\underline{F} = \iint_S \underline{\underline{\sigma}} \cdot \underline{n} \, \mathrm{d}S \; = \pi a^2 \sigma_R \underline{e_z} = 2\pi R d \sigma_R (1 - (d/2R)) \underline{e_z} \tag{7}$$

It is worth noting that in Equation (7) only R and d come into play and not ρ and δ although the integration was carried out over S. Comparing Equa-

tions (6) and (7) leads to the simple result that the above defined apparent crushing strength is equal to the Rankine limit $\sigma_c = \sigma_R$. Equation (7) can be used to evaluate σ_c from the load/penetration curves shown in Figure 3(a). A good agreement is obtained when $\sigma_c = -6.3$ MPa. The same estimate was obtained in a nail-pull test on the same material [6].

The picture is not yet complete in the sense that the abrupt transition from elastic to crushed regimes is not justified. One such justification may be provided by the stress-strain law schematically sketched in Figure 6. Beyond the crushing limit, the stress is softening and an unstable strain interval occurs. As shown on the graph, for intermediate strains, a two-phase regime takes place where part of the volume is crushed and part is elastic. This is a well-known phenomenon leading to strain localization [31]. This regime exists only up to point B where the entire volume has been crushed. Increasing the (compressive) strain further leads to a homogenous densification where the mesoporosity is progressively filled with smaller and smaller fragments at increasing loads.

This pictorial description is a simple scalar view point. In terms of modeling, the (tensor) flow rule has to be specified. A natural guess is to assume that the normality law is obeyed, which is the direction of plastic flow at point A, where Rankine criterion is reached, which is parallel to the normal to the limit stress, i.e., the strain rate direction is that corresponding to uniaxial compression along the direction of the minor principal stress[1]. Because the constitutive law by itself is unstable, the amplitude of the strain jump

[1]the usual convention of counting positive (resp. negative) tensile (resp. compressive) stress is followed herein

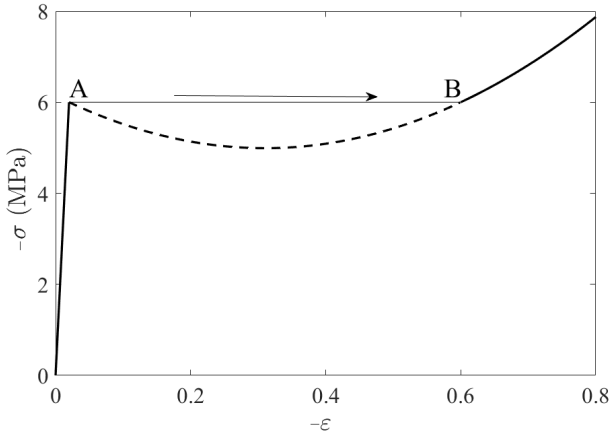

Figure 6: Schematic plot of the constitutive law. The elastic regime (OA) ends with a Rankine failure criterion. Past this point, the material softens and hence an unstable branch shown as a dashed line cannot be observed. Instead the material exhibits a two-phase (E and C) partition, corresponding to points A and B, at fixed macroscopic stress, so that the macroscopic strain is only apparent. Beyond point B, the material response is stable again

from A to B (i.e., states E to C) has to be specified. It has been argued that this jump corresponds to erasing the mesoporosity, that is $\Delta\epsilon_{nn} = \log(1-\phi)$, so that only the position of the front from E to C remains to be determined. Its velocity along the direction of minimum principal strain times the strain jump $\Delta\epsilon_{nn}$ is equivalent to the plastic strain rate in standard plasticity.

This simple picture is at this stage a speculation, which is consistent with the observed indentation date. Yet it is necessary to substantiate it with additional analyses. Thus the indentation test is revisited based on tomographic imaging and DVC so as to evaluate the local strains close to the crushing boundary. Further a macroscopic oedometric test and a uniaxial compression test will also be carried out to validate these statements.

4. Displacement Field Measurements via DVC

Global digital volume correlation has been used for measuring 3D displacement fields. A regular mesh with 8-noded cube (C8) elements was first used (i.e., C8-DVC [30]). The displacement of the n-th volume is evaluated with respect to the initial volume (in the undeformed state). The volume of interest has a size of $576 \times 576 \times 256$ voxels or $6.9 \times 6.9 \times 3.07$ mm^3. The size of C8 elements is $\ell = 8$ voxels or 96 μm. This choice has led to more than 490,000 unknown degrees of freedom. This type of technique yields trustworthy displacements [5] but the measurement uncertainty is too high (i.e., of the order of 0.4 voxel for the displacement, and 2.5% for strains) to yield meaningful strains since they remain very low in magnitude away from the contact zone. The strain uncertainty can be reduced using larger element sizes but at the expense of a larger systematic error due to the steep gradients expected in the vicinity of the indentation zone. Therefore, it is concluded that such a classical methodology cannot be followed to determine strains especially at the boundary of the domain of interest with sufficient reliability and hence a different strategy is proposed.

To evaluate strains and possibly stresses, a reduced basis, which is adapted to the indentation test, is designed [5] for an accurate description of the kinematics of the indentation test especially at the interface of the crushed area and the remainder of the sample that is assumed to behave elastically. A significant reduction in the number of degrees of freedom results from the fact that some information about the sought fields and the constitutive law of the material is available *a priori*. Tomographic findings (Figure 5) show that the indentation of plaster proceeds by the progressive growth of the crushed

zone under the indenter, while the remainder of the sample is considered to be intact. Finite element simulations will be used to construct the reduced basis. The advantage is that the computed displacement fields also satisfy static admissibility so that stress fields can be extracted from the measured fields.

The boundary conditions used in the simulations consist of (i) a rigid body motion of the bottom face of the sample. It is adjusted from a rough analysis via C8-DVC. The estimate of this field is conducted in an area remote from the compacted zone (Figure 7(a)); (ii) stress-free surfaces outside the compacted area; (iii) the boundary of the moving compacted area is searched in a shape compatible with a simple displacement expansion on a truncated spherical harmonic basis.

The library of displacement fields used to describe the displacement of the boundary of the compacted zone is initially limited to axisymmetric contributions

$$\begin{aligned} u_x(a_i,\varphi,\theta) &= w(a_i,\theta)\cos(\varphi)\sin(\theta) + v(a_i,\theta)\cos(\varphi)\cos(\theta) \\ u_y(a_i,\varphi,\theta) &= w(a_i,\theta)\sin(\varphi)\sin(\theta) + v(a_i,\theta)\sin(\varphi)\cos(\theta) \\ u_z(a_i,\varphi,\theta) &= w(a_i,\theta)\cos(\theta) - v(a_i,\theta)\sin(\theta) \end{aligned} \tag{8}$$

where θ and φ are the polar and azimuthal angles (Figure 7(b)). Both fields v and w are linear combinations of the unknown amplitudes a_i

$$\begin{aligned} w(a_i,\theta) &= a_1 + a_2\cos(\theta) + a_3\cos(2\theta) + a_4\cos(3\theta) \\ v(a_i,\theta) &= a_5\sin(\theta) + a_6\sin(2\theta) + a_7\sin(3\theta) \end{aligned} \tag{9}$$

where a_i $(i = 1,\ldots,7)$ denote the amplitudes of the fields to be identified. In addition to these fields, two other fields resulting from shear forces in the transverse plane (i.e., x and y directions) induced by the indenter on

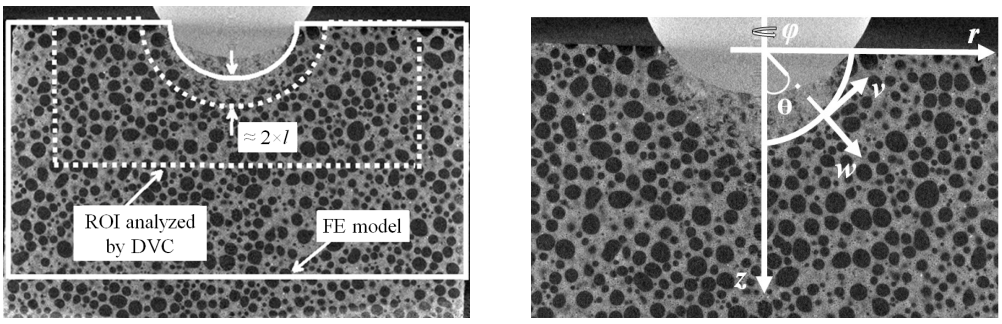

(a) (b)

Figure 7: (a) The analyzed region of interest for digital volume correlation is shown as a dotted line. It is chosen to stay away from the compacted zone where DVC is bound to fail. The zone in which the boundary conditions are determined for the reduced basis is depicted by a solid line. In contrast to the previous domain, it lies inside the compacted zone so that the displacement over the ellipsoidal boundary under the indenter is to be interpreted as a continuation of the elastic problem, and not a physically accessible part of the boundary. ℓ denotes the element size used in DVC analysis. (b) Coordinate system used in the DVC analysis

the specimen are also calculated numerically. Their amplitudes are denoted a_8 and a_9, respectively. These two components are not axisymmetric and are generated by prescribing to all nodes of the hemi-ellipsoidal cap area a uniform displacement along x and y. It was shown that this reduced library of displacement fields was sufficient to describe indentation tests on lightweight gypsum [5].

3D numerical simulations of the indentation test were performed using the commercial software Abaqus. In the FE model, the displacements are prescribed along a surface that is pushed *inside* the crushed zone as shown schematically in Figure 7. The radius is artificially reduced by about 20 voxels. It is clear that this boundary displacement is not to be considered as an

actual displacement. It is rather a mathematical continuation that will allow to probe stresses or strains at any chosen position of the actual boundary. The only limitation to the existence of such a prolongation would be the existence of a singularity that is not anticipated in the immediate neighborhood of the pore collapse boundary. Since no sign of deviation from linear elasticity is observed, it is assumed that the plaster behavior outside the crushed zone remains linear elastic with Poisson's ratio $\nu = 0.15$. Note that the Young's modulus is not needed since Dirichlet boundary conditions or free surfaces are considered. Figure 8 shows the model used in the simulations in which the whole sample is considered. The mesh using tetrahedral elements is illustrated in Figure 8(a). Near the boundary of the crushed zone, the size of the elements is about 100 μm (or 8 voxels). The boundary conditions for the simulations are shown in Figure 8(b).

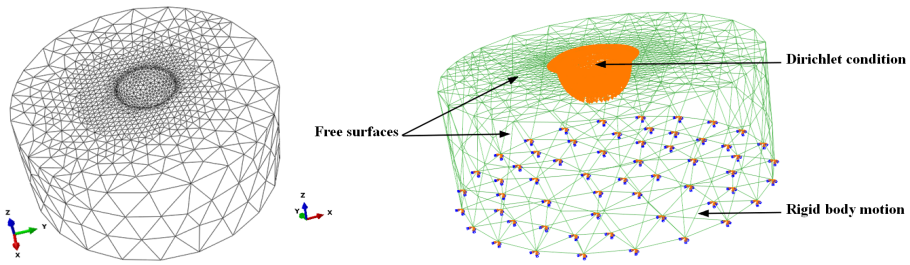

(a) (b)

Figure 8: FE model used to construct the reduced kinematic basis for DVC analyses. (a) Finite element mesh, (b) boundary conditions

>From the finite element simulations, new displacement fields defined at the level of each voxel are obtained (so that the mesh is no longer required for subsequent DVC analyzes). However, as each displacement field extends over the entire region of interest, the problem to solve at each iteration is

global and its size is modest (here 9×9) since the number of fields that make up the reduced basis is equal to 9.

Let us stress the fact that the analyzed domain for DVC is not coincident with that used in the FE analysis. In the immediate vicinity of the indentation zone, a mask is used not to be affected by the crushed region where DVC is expected to fail. However, even if this crushed domain is not taken into account for the determination of the displacement field, the continuation of the displacement field in this region may be used in order to reveal more markedly the boundary of the crushed domain.

As the compacted region lost its initial microstructure, the correlation residuals significantly increase in that area and the displacement field remains undetermined. Correlation residuals provide a very good estimator of the size and shape of the compacted area for *each* voxel, which allows for a detailed description of the boundary area between the compacted zone and the undamaged sample. The change of the crushed area ahead of the indenter is illustrated in Figure 9. 3D renderings of residuals and their average value provide objective indications of measurement quality. They also allow the assumption of elastic behavior outside the compacted area to be validated. The average residual for the last scan is of the order of 3.3 % of the gray level dynamic range (the volume of interest has a size of $400 \times 400 \times 288$ voxels^3 or $4.8 \times 4.8 \times 3.46$ mm^3) to be compared with 2.5 % for the first scan for which no crushing is observed. Let us note that the residuals are also high along the rotation axis. This corresponds to a well-known artifact of the tomographic reconstruction due to detector imperfections that are not averaged out for voxels close to the rotation axis.

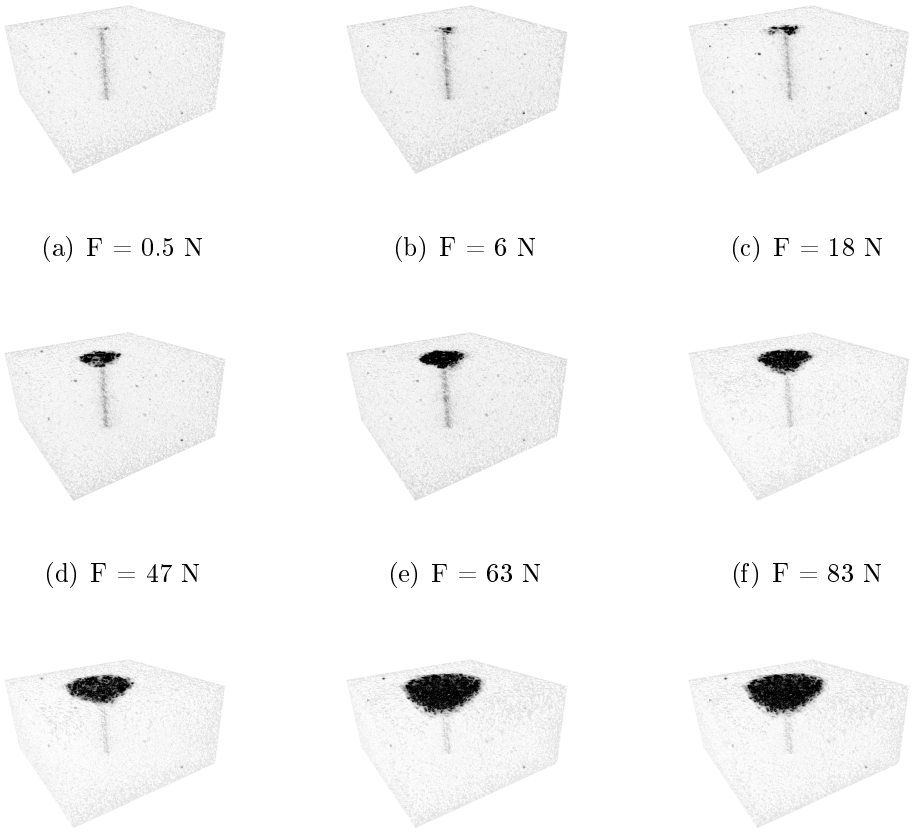

(a) F = 0.5 N (b) F = 6 N (c) F = 18 N

(d) F = 47 N (e) F = 63 N (f) F = 83 N

(g) F = 100 N (h) F = 135 N (i) F = 145 N

Figure 9: 3D rendering of the thresholded correlation residuals showing the development of the crushed zone during the indentation test. The reconstruction artifacts close to the rotation axis are also observed

Let us stress that the proposed procedure allows rather low strain and stress levels to be estimated. At the edge of the collapsed region, the minor principal strain is of order 10^{-2} with a strain uncertainty less than 2×10^{-4}, a value that would not be measurable without the recourse to FE modeling.

5. Identification of Local Failure Criterion

The previous analysis has shown that the material microstructure in the crushed region can no longer be registered with the pristine material. Consequently, the measured fields are only evaluated up to the transition between the two zones. The crushing criterion is identified by extracting meaningful quantities at the boundary. The Young's modulus is first evaluated by matching the measured penetration force with the resultant force calculated along a surface containing the indented area, exploiting the linearity of the constitutive law. The value of $E = 400$ MPa results from this procedure.

>From the measured displacement fields, the components of elastic strains and stresses are deduced especially at the boundary of the compacted area. This is possible since the reduced basis also satisfies static admissibility and the constitutive equation is linear elastic. Figure 10 shows the three eigen stress fields estimated in the volume of the sample. It is worth noting that the stress field is not axisymmetric, which is due to the side motion of the indenter during penetration because of e.g., imperfect parallelism of both sides of the sample after planing, machine rigidity, heterogeneity of the material, friction. The proposed procedure shows that the stress fields are much more complex than what is traditionally assumed in perfect spherical indentation.

The stress fields having been identified in the sample, they are also evaluated at the boundary of the crushed zone. The latter is assumed to be an ellipsoidal surface estimated from the previously shown DVC residual fields. Figure 11 shows the surface (in red) for different levels of the minor principal stress. In the same figures, the 3D rendering of the thresholded correlation

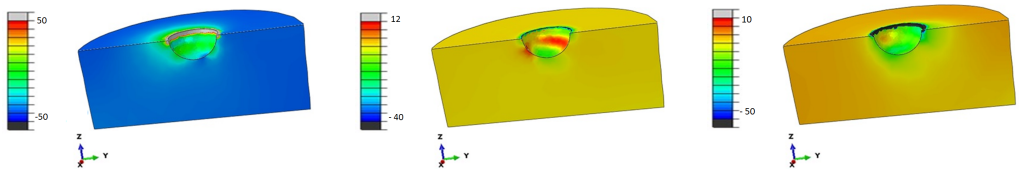

(a) (b) (c)

Figure 10: Stress field extracted from the DVC measurements with the reduced basis (a) major, (b) intermediate, (c) minor eigen stress fields. The color bars indicate the stress magnitude expressed in MPa

residuals (in green) depicts the limit of the crushed zone. The reconstruction artifacts close to the rotation axis are also observed in the correlation residuals. There is a good agreement between the two surfaces especially for the value of the minor principal stress equal to -6 MPa.

6. Oedometric Tests

The previous analysis is based on a small scale test where characteristic sizes were close to those of the microstructure. It is proposed to consider a more macroscopic test where the previous macroscopic law is evaluated. To this end, an oedometric test is carried out. Plaster foam specimens are 8-mm diameter and 10-mm thick cylinders extracted from the core foam with an annular cutter.

The oedometric apparatus consists of a circular PMMA ring containing a core foam sample (Figure 12(a)). The sample is loaded only in the vertical direction, with the piston, by applying increments of load until a desired stress level is reached. The complete stress state of a sample in the apparatus is not known. The only known information is the axial stress. Regarding

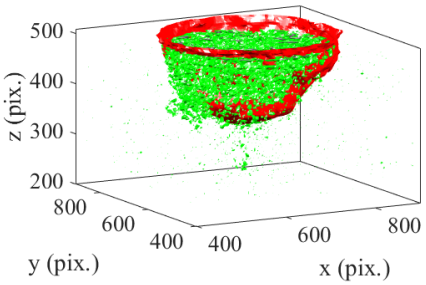

(a) −5 MPa

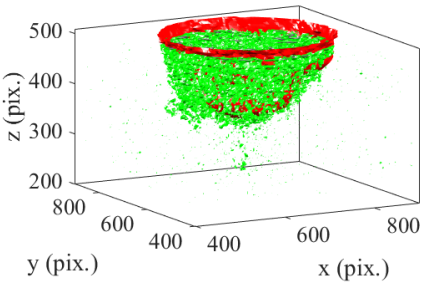

(b) −6 MPa

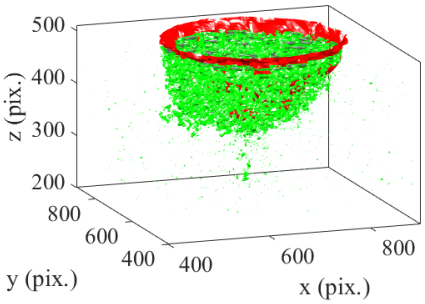

(c) −7 MPa

Figure 11: Surface (in red) for different levels of the minor principal stress. 3D rendering of the thresholded correlation residuals (in green) showing the limit of the crushed zone. The reconstruction artifacts close to the rotation axis are also observed in the correlation residuals

strains, the axial levels are measured as the displacement of the top cap divided by the sample height, while the lateral strain is very small because of the confinement due to the PMMA ring (i.e., $\epsilon_r \approx 0$, see Figure 12(b)). The *in-situ* oedometric test is quasi-static with a stroke rate of 10 μm/s. Two samples were stacked and covered with teflon film to minimize friction between the sample and the wall of the oedometric device. A cylindrical core

foam specimen with a diameter of 8 mm and height of 20 mm was enclosed in a PMMA ring.

The sample was imaged in its initial state (i.e., no applied load) and for several levels of compressive loading. After each load increment, the crosshead was stopped and the next scan was performed. The experiments were conducted on the NSI-X50+ tomograph of LMT, with the following acquisition parameters: 180-kV beam voltage, 120-μA electron current, 11.7-μm resolution. 1,200 radiographs were acquired over a 360° rotation for each scan. The total duration of a single scan is about two and a half hours. Figure 12(c) shows a section of the sample in its initial configuration.

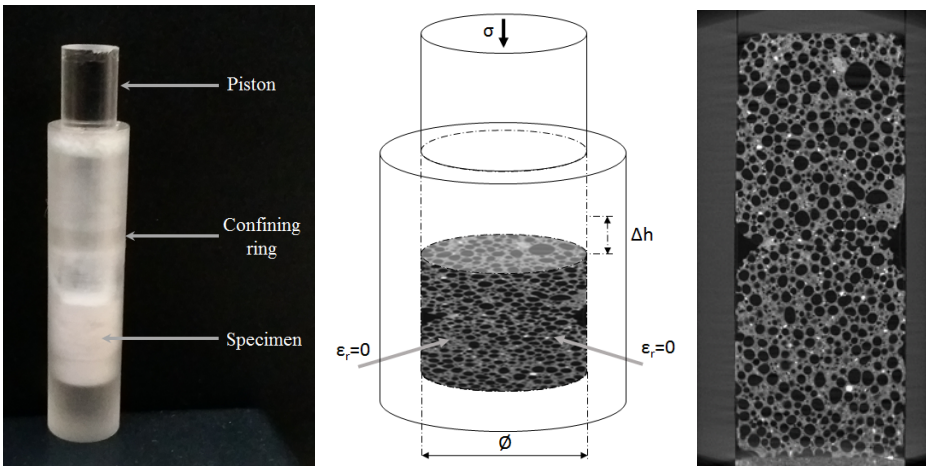

(a) (b) (c)

Figure 12: (a) Oedometric setup. (b) Schematic drawing of the oedometric device. (c) Vertical section of the sample in the oedometric set-up in its initial state (i.e., no applied load)

The observed macroscopic stress-strain response is shown in Figure 13. The strain is the (logarithmic) Hencky description. In a semi-log scale, past the initial elastic (and sample/set-up adaptation), two regimes are observed.

The first one displays a slow compressive stress increase up to a strain of the order of -0.55, which is consistent with the observed strain jump from E to C. At this point, the stress level is close to -6 MPa, again close to the previous estimate of Rankine's limit (see point B in Figure 6, and Equation (7)). In the second regime, a more rapid increase (in absolute value) of the stress with strain suggests that a different mechanism is at play, consistent with the expectation of a stable densification of the finer porosity.

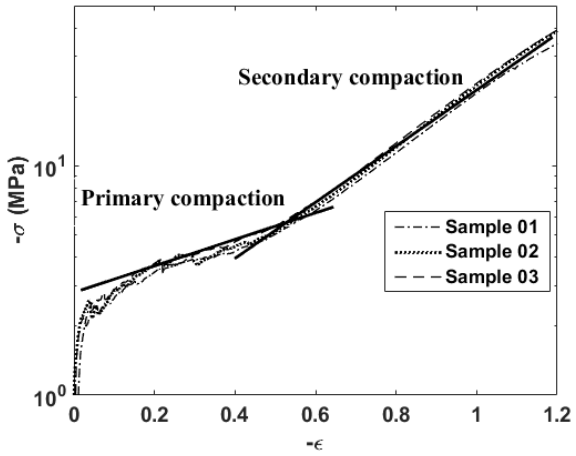

Figure 13: Stress-strain response as measured in oedometric compression

What is however contrasting with the previous expectation is that the initial stage of densification starts at a low stress level (about -2 MPa) and progressively increases, whereas a constant plateau stress at about -6 MPa would be expected following the constitutive law schematically depicted in Figure 6. In order to elucidate this puzzle, tomographic observations of the sample at intermediate stages of loading (i.e., apparent strain of -0.18, -0.4 and -0.6) were performed.

Figure 14 shows an axial section through the sample at these three strain

levels. In the first two images (a) and (b), the material appears very heterogeneous, with crushed plaster along failure surfaces, again in agreement with an unstable constitutive law exhibiting a softening part. However, the local-

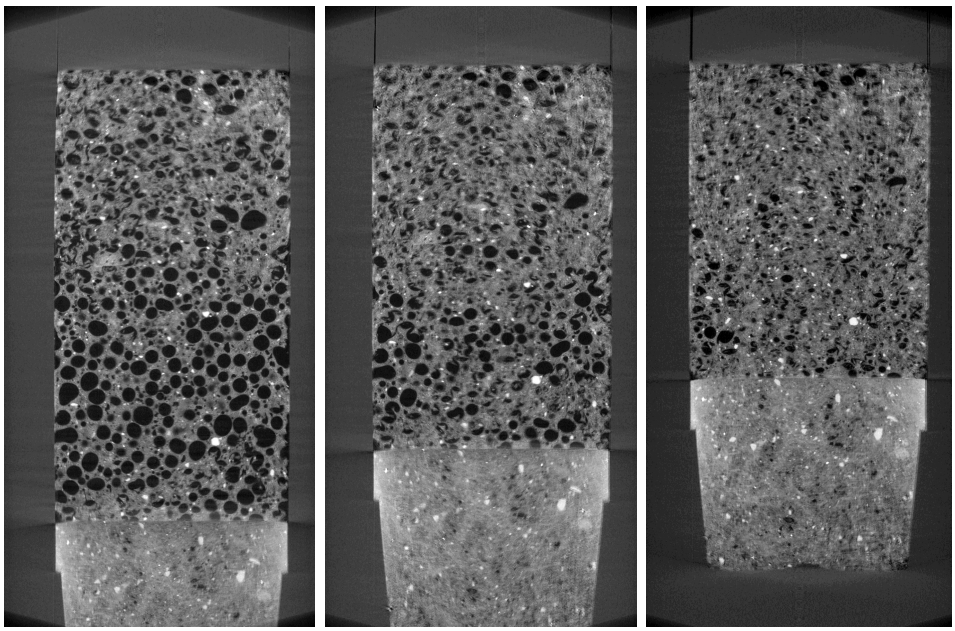

(a) (b) (c)

Figure 14: Sections of the sample in the oedometric set-up, for a mean strain of $\epsilon = -0.18$ (a), $\epsilon = -0.4$ (b), and $\epsilon = -0.6$ (c)

ization patterns are not planes orthogonal to the compression axis. Rather inclined shear failures are observed. A possible reason for the occurrence of such bands is that although the test is close to oedometric, it cannot be perfect in the sense that plaster (and plaster foam) is a brittle material, and hence it is very difficult to have a tight fit of the sample with its casing. As soon as some play is introduced, the initial stage of the test is more comparable to uniaxial compression rather than oedometric. Therefore shear

localization is envisioned as an early stage of failure.

In order to confirm this hypothesis, regularized DVC [19, 35] was used. The volume of interest has a size of $320 \times 320 \times 320$ voxels or $3.75 \times 3.75 \times 3.75$ mm^3. The size of C8 elements is $\ell = 10$ voxels or 117 μm. In the present case, a regularization length of $\ell_{reg} = 40$ voxels was used. Figure 15 shows the DVC results obtained for the first scan ($\epsilon_v > -0.2$). Figure 15(a) and (b) display 3D renderings of respectively the reference and the deformed states. Figure 15(c) shows the gray level residuals (RMS = 6.8 gray levels). The shear bands are clearly revealed on this field. The major principal strain (Figure 15(d)), ϵ_{eq}, shows that localization occurs with a complex pattern. Let us note the existence of a crack parallel to the loading direction (z-axis) has developed in the first step of loading followed by the onset of shear bands at 45 degrees.

After a small slip along the shear surface, an acute portion of the sample is pressed against the piston and crushing is promoted at a lower pressure level than expected without symmetry breakage. The difficulty of dealing with an unstable constitutive law is that many mechanisms may compete to produce compaction at a low stress level. However, for an apparent strain of -0.6 (i.e., the last tomographed state) the entire sample microstructure is more homogeneous, being uniformly crushed. Figure 16 shows the DVC results obtained for a scan whose absolute volumetric strain exceeds 0.6 (i.e., $\epsilon_v < -0.6$). Figure 16(a) and (b) shows respectively 3D renderings of the correlation residual and incremental major principal strain. These computations are very complex as they are performed in the crushed state of the material. However the residuals are not too high to disqualify the reported

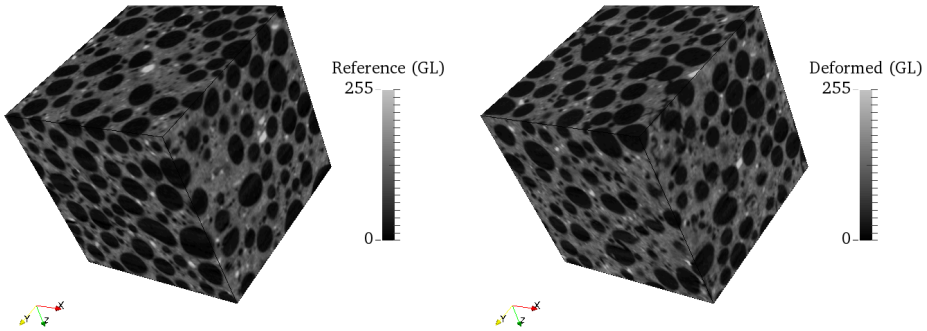

(a) Reference configuration (b) Deformed configuration

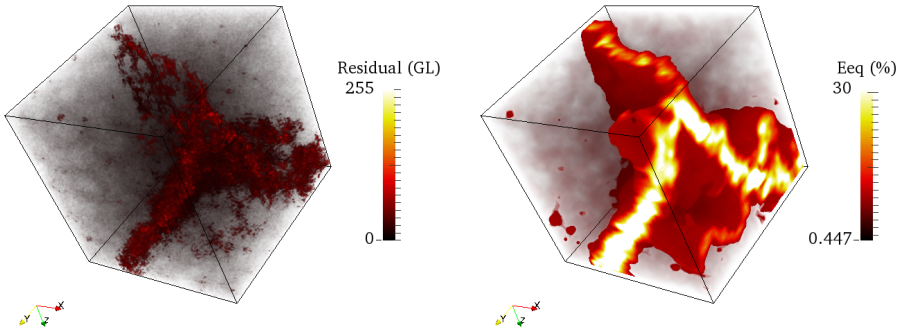

(c) Correlation residual (d) Major principal strain ϵ_{eq}

Figure 15: 3D renderings of the microstructure of foamed plaster to be subjected to a oedometric test (a), first deformed configuration (b), gray level correlation residual (c), and major principal strain ϵ_{eq} (d)

results. Both fields show that the test at this stage of loading still exhibits large uniformly distributed strain fluctuations.

Albeit the macroscopic oedometric response is not the anticipated perfect

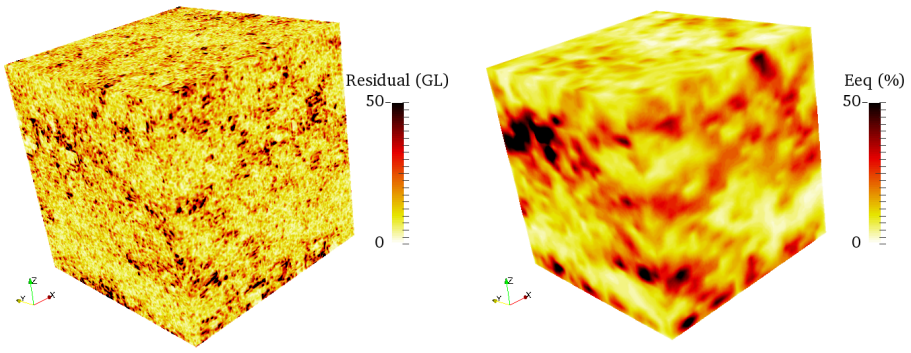

(a) Correlation residual (b) Major principal strain ϵ_{eq}

Figure 16: 3D renderings of correlation residual (a) and major principal strain ϵ_{eq} (b) of an incremental DVC calculation at the end of the oedometric test

stress plateau, the above observations is consistent with the proposed behavior for plaster foam. In order to prevent the occurrence of a large shear band to by-pass the peak stress (point A in Figure 6), a uniaxial compression is performed along the thickness direction over a wider specimen. The natural thickness of the sample h is that of the plasterboard itself, hence $h = 13$ mm. A large width/thickness aspect ratio sample makes uniaxial compression a perfect oedometric test, apart from the vicinity of free edges.

Such tests have been conducted with three samples of size $L \times L$, where $L = 40$ mm. It is observed that very early on, triangular prisms separate from the rest of the structure all along the free edges. This is again a manifestation of shear localization. However the aspect ratio of the specimen limits the detrimental effect of such damage on the further exploitation of the test. The load versus displacement response displays an almost perfect

plateau that corresponds to the progressive densification of plaster foam core. The evaluation of the stress corresponding to this plateau is however to be performed over the effective supporting cross sectional area, i.e., where edge effects have been accounted for. For prisms produced by shear bands roughly oriented at $\pi/4$ with respect to the compression axis, the width of the edge prism is $h/2$ leading to a rough estimate of the supporting cross-section of the order of $(L-h)^2$. Using the latter estimate gives again a critical compaction stress of ≈ -6 MPa (see Figure 17); a value consistent with the indentation estimate of the crushing strength based on Rankine's criterion.

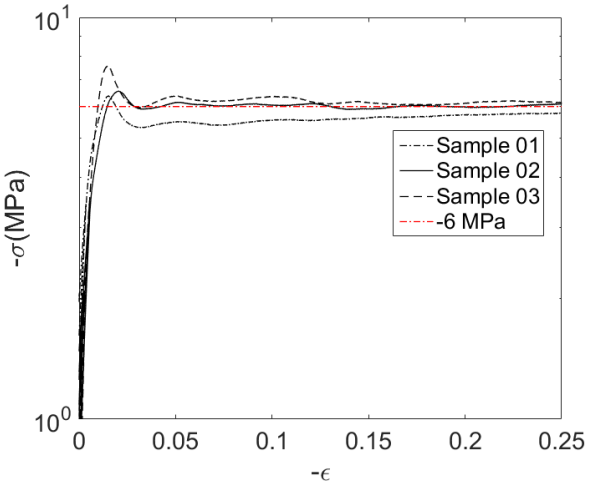

Figure 17: Stress-strain response measured in uniaxial compressive tests

Brittle fracture, as a result of the weakest link mechanism [15, 29, 37], is known to display systematic size effects. In the present case, because the elementary phenomenon is the brittle fracture of walls between pores, one may wonder whether pore collapse shows such a size effect. The fact that the E-C transition takes place along a surface that sweeps through the entire

solid is a crucial difference with tensile fracture, and suggests that no size effects are to be expected.

In order to validate this aspect, it is to be noted that the relevant size has to be the area of the pore collapse front, and in the above reported experiments, this area ranges from a small value for indentation, up to very large values for uniaxial compression. For the former, this surface is a portion of sphere with an effective radius ρ above computed (see Section 3.1). For the largest indentation depth observed herein, this area A_{indent} is estimated as ≈ 25 mm^2. In uniaxial compression, the E-C transition takes place along a plane normal to the compression axis, and has an area of $A_{compress} \approx 1600$ mm^2. These two extreme cases correspond to a ratio of area of about 64, and yet the experimental data are consistent with the same value for the compressive strength. Thus it is concluded that, within the present data uncertainty, no systematic size effect can be detected.

7. FE Simulations

To complete the characterization of the material, FE simulations are carried out. The goal is to investigate whether existing constitutive laws [18, 22] can predict the behavior of foamed plaster in terms of global load-displacement response, and the crushed zone that develops during indentation and oedometric tests. In the numerical simulation foamed plaster is considered as a continuum solid with mechanical properties representative of both the solid and porous phases.

7.1. Mohr-Coulomb Model

The constitutive law used herein to model the behavior of plaster is based on Mohr-Coulomb criterion, which relates the shear and normal stresses in the material at failure yielding

$$\tau = c + \sigma_n \tan(\phi) \tag{10}$$

where τ is the shear stress, σ_n the normal stress, c the cohesion of the material, and ϕ the friction angle.

The indentation test was modeled by the FE software Abaqus using large deformation computations. The indenter was considered rigid. Loading was achieved by prescribing a quasi-static vertical displacement to the indenter. The sample was considered as clamped on its base. The contact between the rigid indenter and the specimen was assumed to be frictionless and was modeled using the slideline approach with a penalty formulation [39]. The finite element mesh used in the computation is shown in Figure 18. It is made of 2,232 axisymmetric linear triangular (i.e., CAX3) elements. The mesh density is deliberately higher in the vicinity of the contact region under the indenter. The boundary conditions used in the computation are illustrated in the reference and deformed configurations. Mohr-Coulomb parameters used in FE calculation are summarized in Table 2, where ψ is the dilatancy angle. The parameters used in this study are close to those identified by Clément et al. [10]. The latter study was carried out on foamed plaster with a lower porosity range (i.e., 56 % vol.).

Figure 19 reports the total force acting on the rigid indenter in the vertical direction as a function of the penetration of the indenter in the same

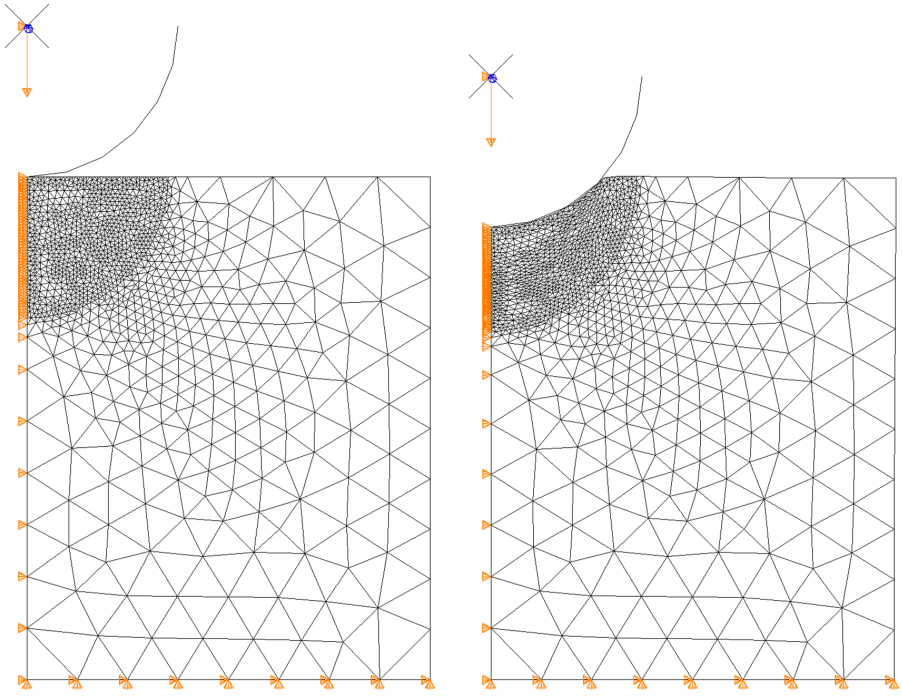

(a) Initial configuration (b) Deformed configuration

Figure 18: FE axisymmetric model of the spherical indentation test. FE mesh and boundary conditions in the initial (a) and deformed (b) configurations

Table 2: Mohr-Coulomb parameters

ϕ ($^\circ$)	ψ ($^\circ$)	c (MPa)
11	1	0.8

direction. The numerical response is in good agreement with the experimental measurement. This result validates the material parameters considered herein.

Figure 20(a) shows the contours of equivalent plastic strain compared with the size of the compacted zone observed *in-situ* for the same penetration.

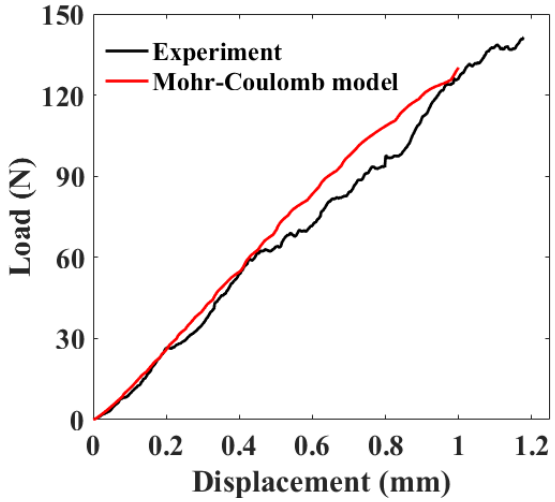

Figure 19: Comparison between numerical and experimental response in terms of load-displacement curve

The pile-up phenomenon is not observed around the indenter, which is in agreement with the experimental observations. It is also noticed that the material directly ahead of the indenter and close to the axis of symmetry shows little or no plastic deformation. It has a conical shape during the indentation process. This phenomenon is *not observed* in the tomographic observations. The model overestimates the dimension of the crushed zone, in particular its depth. Figure 20(b) shows a map of the minor eigen stress in the loaded configuration. For the experimental transition, the corresponding stress level is of the order of -6 MPa.

The transition from intact to crushed states is modeled as progressive and smeared over a wide zone in contrast with the experiment where the transition appears to be very sharp. In particular, no signs of damage or irreversible densification are observed experimentally in the elastic phase even close to

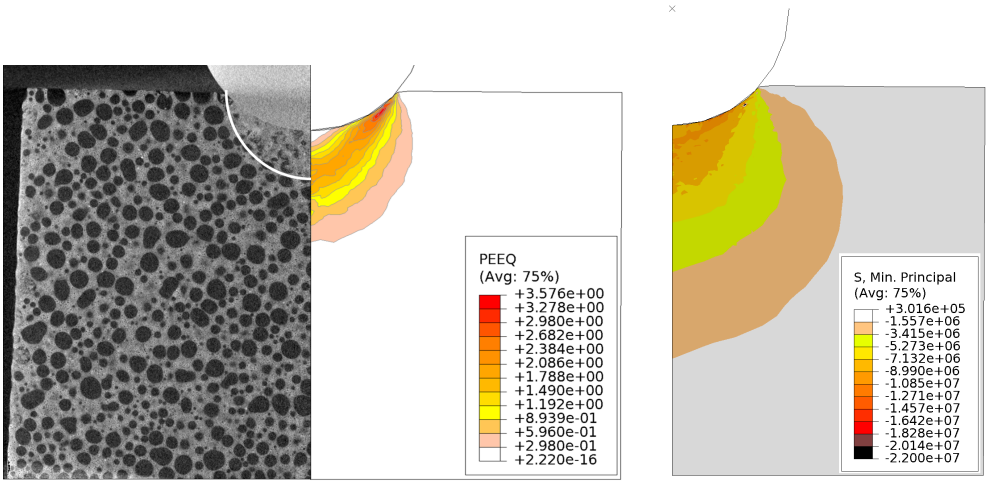

(a) Equivalent plastic strain (b) Minor eigen stress

Figure 20: (a) Compacted zone compared with the equivalent plastic strain. (b) Map of minor principal stress in the loaded configuration expressed in Pa

the crushed zone boundary. Similarly in the experiment, once crushed, it appears that the material density remains constant, so that indentation appears as a "transformation front" moving inside the material but where very little strains can be measured. The contrast with the proposed modeling is striking. However, it is fair to emphasize that the numerical modeling of a constitutive law such as that schematically depicted in Figure 6 is challenging as the introduced softening branch gives rise to a localization of a large plastic ("crushing") strain onto a sharp front.

Last, let us stress the fact that identification of a mechanical behavior from an indentation experiment is an ill-posed problem, and judging only from the quality of the load-penetration curve may lead to fragile conclusions. In this context, *in-situ* tomographic experiments appear to bring a

discriminating piece of information.

7.2. Crushable Foam Model

The oedometric test was also modeled by the FE software Abaqus. The piston was deformable. Loading was achieved by prescribing a quasi-static vertical displacement to the piston. The confining ring was considered as clamped on its base. The contact between the oedometric device and the specimen was assumed to be frictionless and was modeled using the slideline approach with a penalty formulation [39]. Four-node axisymmetric elements (i.e., CAX4R) were used to mesh the model, which is made of 450 elements.

The crushable foam plasticity model [18] available in Abaqus was used. The material input data, i.e., volumetric hardening in the crushable foam model was obtained from the macroscopic material response under oedometric condition. Figure 21(a) shows the calibrated and experimental stress-strain curves. The predicted response by the FE model is in very good agreement with experimental values. It should be noted that such agreement between simulated and experimental curves results from the use of the material data obtained from experimental tests.

The curves correspond to a typical stress-strain behavior for cellular materials having three distinct stages [16]. At stage I, under relatively low loads up to about 0.04 strain, the material is linear elastic. At stage II, under some critical level of load, pore collapse begins due to elastic buckling and/or brittle fracture. The pore collapse front then progresses producing a inclined stress plateau, until relatively large strains (about 0.6 in absolute value). At stage III, the stress then rises steeply as the material densifies, and finally the material reaches bulk-like properties.

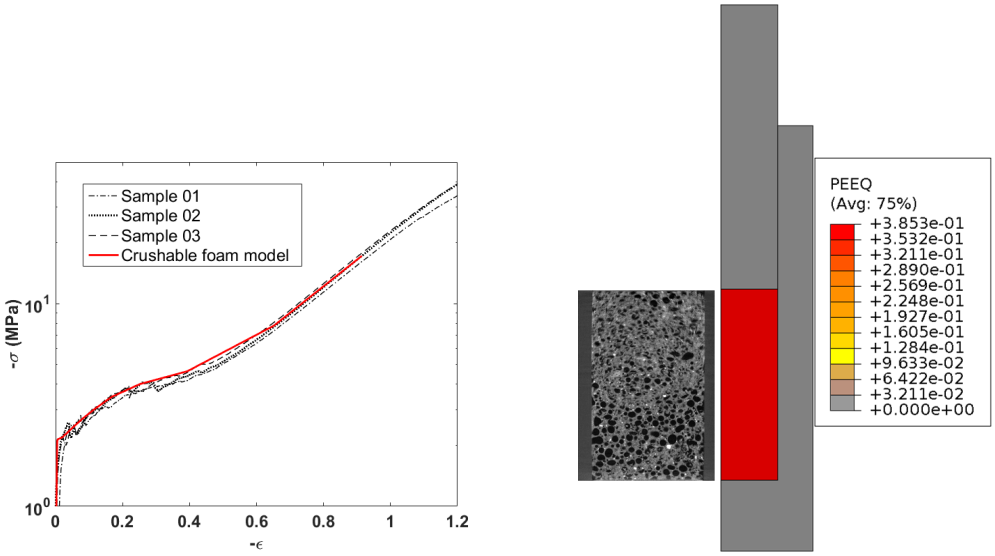

(a) (b)

Figure 21: (a) Calibrated and experimental stress-strain curves of oedometric tests on foamed plaster. (b) Sagittal tomographic section compared with the equivalent plastic strain map

Figure 21(b) shows the contours of equivalent plastic strain compared with the sagittal tomographic section observed in the *in-situ* oedometric test for the same displacement of the piston. The computed equivalent plastic strain field is homogeneous. This phenomenon is not observed in the DVC fields (see Figures 15 and 16). Although the macroscopic behavior is well described, localized and fluctuating patterns observed experimentally at the microscopic scale are not reproduced by the FE model.

8. Conclusion

Foamed plaster has been tested *in-situ* via spherical indentation. Tomographic observations show the formation of a region under the indenter where the brittle foam has been crushed to a state where large pores have disappeared and where density (observed from X-ray absorption coefficient) appears to be extremely uniform. This observation suggests that, once porosity has collapsed, crushed gypsum does not undergo visible further densification. Away from the crushed material, the foam appears (within the present microstructure and strain resolution) as mostly undamaged and devoid of irreversible strain. The transition from the elastic state to the crushed one takes the form of a very sharp boundary on the tomographic images, suggesting an abrupt mechanical transformation between those two states. Indentation proceeds by the progressive growth of the crushed domain inside the intact foam. *In-situ* mechanical tests, in particular indentation tests are well-suited for a comprehensive characterization of the full 3D kinematics and therefore the identification of mechanical properties thanks to digital volume correlation. A constitutive law consistent with the observed crushing mechanism in the indented volume was proposed, which consists of an elastic regime limited by Rankine's criterion, and followed by a softening behavior prior to a secondary (hardening) densification stage of the crushed gypsum foam.

It is shown that despite the fact that a Mohr-Coulomb model reproduces very well the global response of the indentation test (i.e., load-displacement curve), a poorer prediction of the experimental crushed zone is observed. In particular, the transition between compacted plaster and its pristine state is not captured by the model, which predicts a very progressive transition

rather than an abrupt one. Alternatively, the proposed mechanical behavior is challenging on the numerical modeling side, and has not been implemented in the form of a constitutive law.

To validate the proposed description of the behavior, it is important to quantify the stresses and strains at the crushing boundary. However, the microstructure of materials, tomography artifacts and heterogeneity of the test may lead to large uncertainties in the measured fields. A tailored basis of displacement fields for DVC purposes was designed and computed with 3D elastic finite element simulations. The *a priori* information on the mechanical behavior and relevant boundary conditions are exploited in the choice of this reduced basis. It allowed the triaxial stress state to be determined in the transition zone between the compacted zone and the elastic region. These data revealed consistent with Rankine's criterion for the onset of porosity collapse, which is the prevalent failure mechanism in a standardized (nail-pull) test [6].

Additionally, a macroscopic *in-situ* oedometric test was performed. Although different localization modes appear in the sample leading to a premature densification, localized modes were observed in the softening regime, and finally when the entire sample is uniformly crushed, a densification (i.e., hardening) behavior is observed with stress and strain levels consistent with the indentation experiment. It is also found that a crushable foam model is fully consistent with the global response of the material. However, a uniform strain field is predicted, which is not observed experimentally.

Through-thickness uniaxial compression over wide samples shows a behavior consistent with the proposed law with a similar value of the com-

paction strength. It is noteworthy that due to the presence of a softening regime following the beginning of compaction, macroscopic tests are difficult to interpret directly, namely, oedometric tests display strongly heterogeneous localized modes in shear rather than in compaction for stresses below the estimated Rankine stress, and uniaxial compression over wide specimen exhibits significant size effects. In contrast, due to the natural stress gradient resulting from geometry indentation tests stabilize the material response in the form of an abrupt front separating the elastic and compacted material, which propagates through the material as the load increases.

One may anticipate that such a qualitative behavior may hold for a wide variety of porous materials whose skeleton is made of a brittle phase. Indentation coupled with *in-situ* tomographic observation is an outstanding way of quantifying and validating such behaviors.

Acknowledgements

For the completion of this work, AB has been supported by a CIFRE PhD fellowship from ANRT and Saint-Gobain. It is a pleasure to acknowledge useful discussions with R. Gy from Saint-Gobain Recherche. This work has been financially supported by the French Agence Nationale de la Recherche through the "Investissements d'avenir" program (ANR-10-EQPX-37 MATMECA grant). We acknowledge the European Synchrotron Radiation Facility and we would like to thank E. Boller for assistance in using beamline ID19.

References

[1] M.F. Ashby, A.G. Evans, N.A. Fleck, L.J. Gibson, J.W. Hutchinson, and H.N.G. Wadley. *Metal Foams: A Design Guide*. Butterworth-Heinemann, Boston, MA (USA), 2000.

[2] H. Bart-Smith, J.W. Hutchinson, and A.G. Evans. Measurement and analysis of the structural performance of cellular metal sandwich construction. *Int. J. Mech. Sci.*, 43:1945–1963, 2001.

[3] B.K. Bay. Methods and applications of digital volume correlation. *J. Strain Analysis*, 43:745–760, 2008.

[4] A. Bouterf. *Comportement mécanique de la plaque de plâtre étudié par tomographie et essais mécaniques in-situ*. PhD thesis, ENS Cachan, 2014.

[5] A. Bouterf, S. Roux, F. Hild, J. Adrien, and E. Maire. Digital volume correlation applied to X-ray tomography images from spherical indentation tests on lightweight gypsum. *Strain*, 50(5):444–453, 2014.

[6] A. Bouterf, S. Roux, F. Hild, G. Vivier, X. Brajer, and E. Maire. Failure mechanisms of plasterboard in nail pull test determined by x-ray microtomography and digital volume correlation. *Exp. Mech.*, in press (DOI: 10.1007/s11340-016-0168-8), 2016.

[7] J.Y. Buffière, E. Maire, J. Adrien, J.P. Masse, and E. Boller. In Situ Experiments with X ray Tomography: an Attractive Tool for Experimental Mechanics. *Exp. Mech.*, 50(3):289–305, 2010.

[8] J.Y. Buffière, E. Maire, P. Cloetens, G. Lormand, and R. Fougères. Characterisation of internal damage in a MMCp using X-ray synchrotron phase contrast microtomography. *Acta Mater.*, 47(5):1613–1625, 1999.

[9] P. Clément. *Détermination des propriétés mécaniques de céramiques poreuses par essais de microindentation instrumentée sphérique.* PhD thesis, INSA de Lyon, 2013.

[10] P. Clément, S. Meille, J. Chevallier, and C. Olagnon. Mechanical characterization of highly porous inorganic solids materials by instrumented micro-indentation. *Acta Mat.*, 61:6649–6660, 2013.

[11] V.S. Deshpande and N.A. Fleck. Multi-axial yield behaviour of polymer foams. *Acta Mat.*, 49(10):1859–1866, 2001.

[12] J. Desrues and E. Andò. Strain localisation in granular media. *C. R. Physique*, 16:26–36, 2015.

[13] M. Flumiani, T. Elliot, and B. Bruce. *Nail Pull Mechanism as Determined by Computed Tomography.* Private communication, Innogyps Research Center, Canada, 2008.

[14] F. Forsberg and C. R. Siviour. 3D deformation and strain analysis in compacted sugar using X-ray microtomography and digital volume correlation. *Meas. Sci. Tech.*, 20(9):095703, 2009.

[15] A.M. Freudenthal. *Statistical Approach to Brittle Fracture*, volume 2, pages 591–619. Academic Press, New York (USA), 1968.

[16] L.J. Gibson and M.F. Ashby. *Cellular Solids: Structure and Properties.* Cambridge University Press,, Cambridge (UK), 1997.

[17] S. Hall, J. Desrues, G. Viggiani, P. Bésuelle, and E. Andò. Experimental characterisation of (localised) deformation phenomena in granular geomaterials from sample down to inter- and intra-grain scales. *Procedia IUTAM*, pages 54–65, 2012.

[18] A.G. Hanssen, M. Langseth, and O.S. Hopperstad. Crash behavior of foam-based components: Validation of numerical simulations. *Adv. Eng. Mat.*, 4(10):771–776, 2002.

[19] F. Hild, A. Bouterf, and S. Roux. Damage measurements via dic. *Int J. Fract.*, 191:77–105, 2015.

[20] K.L. Johnson. *Contact Mechanics.* Cambridge University Press, Cambridge (UK), 1985.

[21] M.H. Leite and F. Ferland. Determination of unconfined compressive strength and Young's modulus of porous materials by indentation tests. *Eng. Geolog.*, 59:267–280, 2001.

[22] J.P. Magan and P. Mestat. Lois de comportement et modélisation des sols. *Techniques de l'ingénieur, traité Construction*, C218.

[23] M. Mostafavi, D.M. Collins, B. Cai, R. Bradley, R.C. Atwood, C. Reinhard, X. Jiang, M. Galano, P.D. Lee, and T.J. Marrow. Yield behavior beneath hardness indentations in ductile metals, measured by three-dimensional computed x-ray tomography and digital volume correlation. *Acta Mat.*, 82:468–482, 2015.

[24] M. Mostafavi, S.A. McDonald, P.M. Mummery, and T.J. Marrow. Observation and quantification of three-dimensional crack propagation in poly-granular graphite. *Eng. Fract. Mech.*, 110:410–420, 2013.

[25] M. Mostafavi, S.A. McDonald, P.M. Mummery, and T.J. Marrow. Three-dimensional crack observation, quantification and simulation in a quasi-brittle material. *Acta Mat.*, 61:6276–6289, 2013.

[26] E. Olsson and P.-L. Larsson. A numerical analysis of cold powder compaction based on micromechanical experiments. *Powder Technol.*, 243:71–78, 2013.

[27] O.B. Olurin, N.A. Fleck, and M.F. Ashby. Indentation resistance of an aluminium foam. *Scripta Mat.*, 43:983–989, 2000.

[28] P. Paniagua, E. Andò, M. Silva, A. Emdal, S. Nordal, and G. Viggiani. Soil deformation around a penetrating cone in silt. *Géotech. Lett.*, 3:185–191, 2013.

[29] F.T. Pierce. Tensile tests for cotton yarns, v. the 'weakest link' theorems on the strength of long and of composite specimens. *J. Text. Inst.*, 17:T355–T368, 1926.

[30] S. Roux, F. Hild, P. Viot, and D. Bernard. Three dimensional image correlation from X-Ray computed tomography of solid foam. *Comp. Part A*, 39(8):1253–1265, 2008.

[31] J.W. Rudnicki and J.R. Rice. Conditions for localization of deformation in pressure-sensitive dilatant materials. *J. Mech. Phys. Solids*, 23:371–394, 1975.

[32] T.S. Smith and B.K. Bay. *Experimental Measurement of Stains using Digital Volume Correlation*, volume STP 1323. ASTM, West Conshohocken, Pa (USA), 2001.

[33] F.R. Suárez-Rivera, N.G. Cook, G.A. Cooper, and Z. Zheng. Indentation by pore collapse in porous rocks. In *31st US Symp. on Rock Mech.*, volume 671-678, 1990.

[34] D. Tabor. *The Hardness of Metals*. Oxford University Press, Oxford (UK), 2000.

[35] T. Taillandier-Thomas, S. Roux, T.F. Morgeneyer, and F. Hild. Localized strain field measurement on laminography data with mechanical regularization. *Nucl. Inst. Meth. Phys. Res. B*, 324:70–79, 2014.

[36] Y. Vertyagina, M. Mostafavi, C. Reinhard, R. Atwood, and T.J. Marrow. In situ quantitative three-dimensional characterisation of sub-indentation cracking in polycrystalline alumina. *J. Europ. Ceram. Soc.*, 34:3127–3132, 2014.

[37] W. Weibull. A survey of 'statistical effects' in the field of material failure. *Appl. Mech. Rev.*, 5(11):449–451, 1952.

[38] Johnson K.L. Ashby M.F. Wilsea, M. *The Hardness of Metals*. Oxford University Press, Oxford (UK), 2000.

[39] P. Wriggers, T. Vu Van, and E. Stein. Finite element formulation of large deformation impact-contact problems with friction. *Comput. Struct.*, 37:319–331, 1990.

Appendix A: Closed-form solution for the geometrical model

Section 3.1 presented a simple geometrical model showing that the actual indentation of the brittle foam by a rigid sphere of radius R and penetration d, was in fact a self-indentation of the material by the comminuted material. The latter could itself be described by a sphere of radius ρ and penetration δ. In the limit of a small penetration, $d/R \ll 1$ a very simple expression of these effective parameters results from geometrical considerations, $\rho = R\phi$ and $\delta = d/\phi$.

However, in the experiment, the ratio d/R did not remain small, and hence it is worthwhile considering the expressions of ρ and δ without such an approximation. Equations (2) and (3) are rewritten as

$$\begin{aligned} 2\rho\delta - \delta^2 &= 2Rd - d^2 \\ 3\rho\delta^2 - \delta^3 &= \frac{3Rd^2 - d^3}{\phi} \end{aligned} \tag{11}$$

hence

$$\delta^3 + 3d(2R - d)\delta - \frac{2d^2(3R - d)}{\phi} = 0 \tag{12}$$

This cubic equation can be solved analytically providing

$$\delta = (A + B)^{1/3} - (A - B)^{1/3} \tag{13}$$

where

$$\begin{aligned} A &= d^{3/2}\left[(8R^3 + (9/\phi^2 - 12)R^2 d - 6(1/\phi^2 - 1)Rd^2 + (1/\phi^2 - 1)d^3)\right]^{1/2} \\ B &= d^2(3R - d)/\phi \end{aligned} \tag{14}$$

One may note that from these expressions, even for a deep indentation $d/R = 0.1$ (resp. 0.2) the error on δ using the linear approximation $\delta \approx d/\phi$ does not exceed 5 % (resp. 9 %).

The undamaged-crushed (E-C) boundary is a portion of sphere whose radius is

$$\rho = \frac{2Rd - d^2 + \delta^2}{2\delta} \tag{15}$$

□